Electronic Supplementary Material (ESI) for Materials Horizons.

Supporting information

The mechanisms behind extreme susceptibility of photon avalanche emission to quenching

Martyna Majak*, Małgorzata Misiak, Artur Bednarkiewicz*

Institute of Low Temperature and Structure Research, Polish Academy of Sciences, ul. Okólna 2, 50-422 Wroclaw, Poland

Corresponding authors: martynamajak97@gmail.com ; a.bednarkiewicz@intibs.pl

Contents

Sample characterization

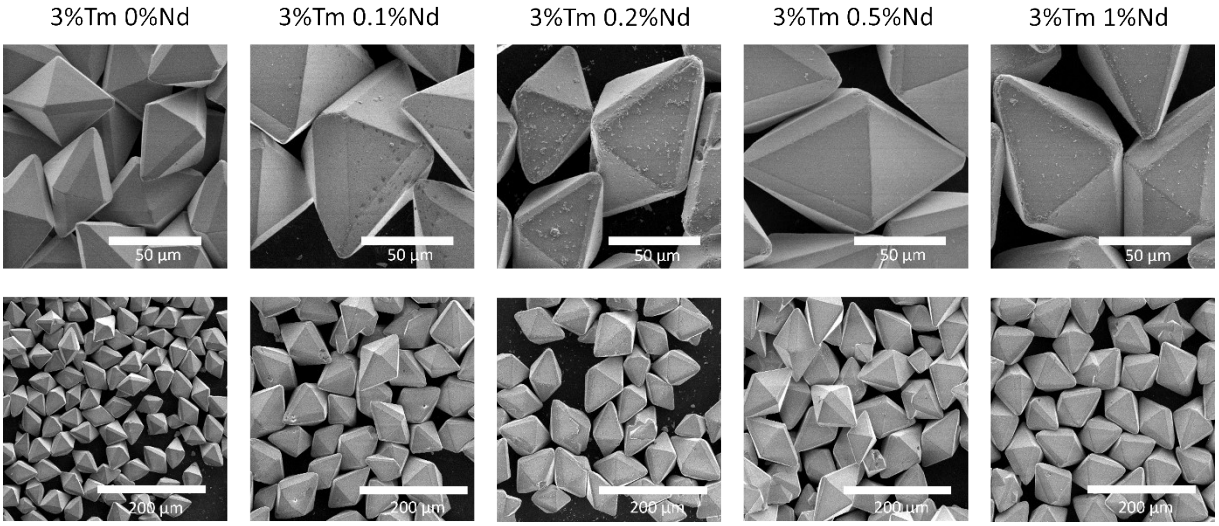

Figure S1 *SEM images for different resolutions for 0, 0,1, 0,2, 0,5 and 1% Nd^{3+} ion concentration.*

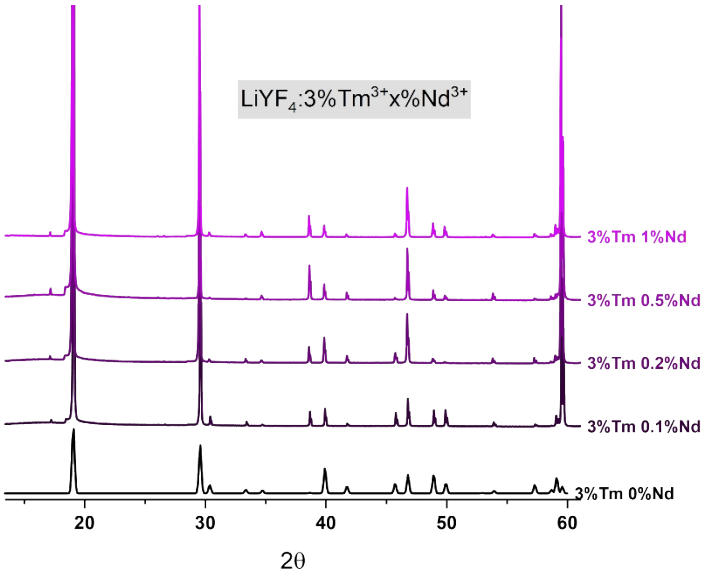

Figure S2 *XRD pattern of $LiYF_4$:3%Tm^{3+}*

Optical setup and experimental methods

Pump power dependent PA and PA spectra

Pump power dependent PA measurements were conducted on a dedicated experimental setup using butterfly single mode laser diode 1059 nm working in a steady-current mode with current set at 770mA (1064CHP, 3SPTechnologies) as an excitation source. Laser diode is integrated to the controller maintaining constant temperature and current (CLD 1015, Thorlabs) and led to the system through a single mode polarization maintaining fiber and collimator (C, F280APC-1064, Thorlabs).The laser beam is focused to a sub-diffraction-limited diameter of 1.2 μm, enabling the excitation of a small volume within the microcrystal (c.a. 60 μm). The automatized gradient neutral density filter (NDC-100C4M, Thorlabs) and the set of neutral density filters (NDUV06, NDUV10, NDUV20, Thorlabs) were placed in the optical path of the laser beam to precisely change the excitation power. A small fraction of the laser beam is reflected from a beam splitter and is directed to the power sensor (S121C+PM100, Thorlabs) reading the reference power, which allows for determination of the excitation beam power. The 1059 nm laser beam is reflected from the short-pass dichroic mirror (DMSP900R) and directed towards the inverted microscope port (Nikon Ti-2 Eclipse). The beam is further focused on the sample through the objective lens (O, Plan Apo λ 40x, NA=0.95, Nikon). Sample emission is collected through the same objective and directed to the short-pass dichroic mirror (DMSP900R), at which emission beam is transmitted. If the emission intensity exceeds detector capability, the emission beam can be attenuated via neutral density filters. After that, the emission beam directed is at a flipped mirror (FM). While FM is set the beam is guided through fibers to the two photomultiplier tubes (PMT, PMT1001M, PMT2001M, Thorlabs) connected to the photon counter (quTAG, quTools). PMTs are cooled by a Peltier system to the temperature of 13 ^{o}C to reduce dark currents. Two spectral channels are measured by PMTs by using a dichroic cube with a dichroic mirror spectrally splitting the beam (FF756 SDi01 Semrock) and bandpass filters (811AF22, 475BP30, Omega Optical). When FM is lowered the emission beam is led to the commercial Czerny-Turner spectrograph (Shamrock 500i) consisting of the cooled down to -60 ^{o}C camera (Newton 920P-BEX2-DD CCD). PA pump-probe measurement is realized via arbitrary waveform generator (integrated in Handyscope 5 USB oscilloscope, TiePie) modulating the voltage of the laser diode to operate in pulse mode. To maintain consistency in the measurements, the power was incrementally increased with delay time, ensuring a constant average power.

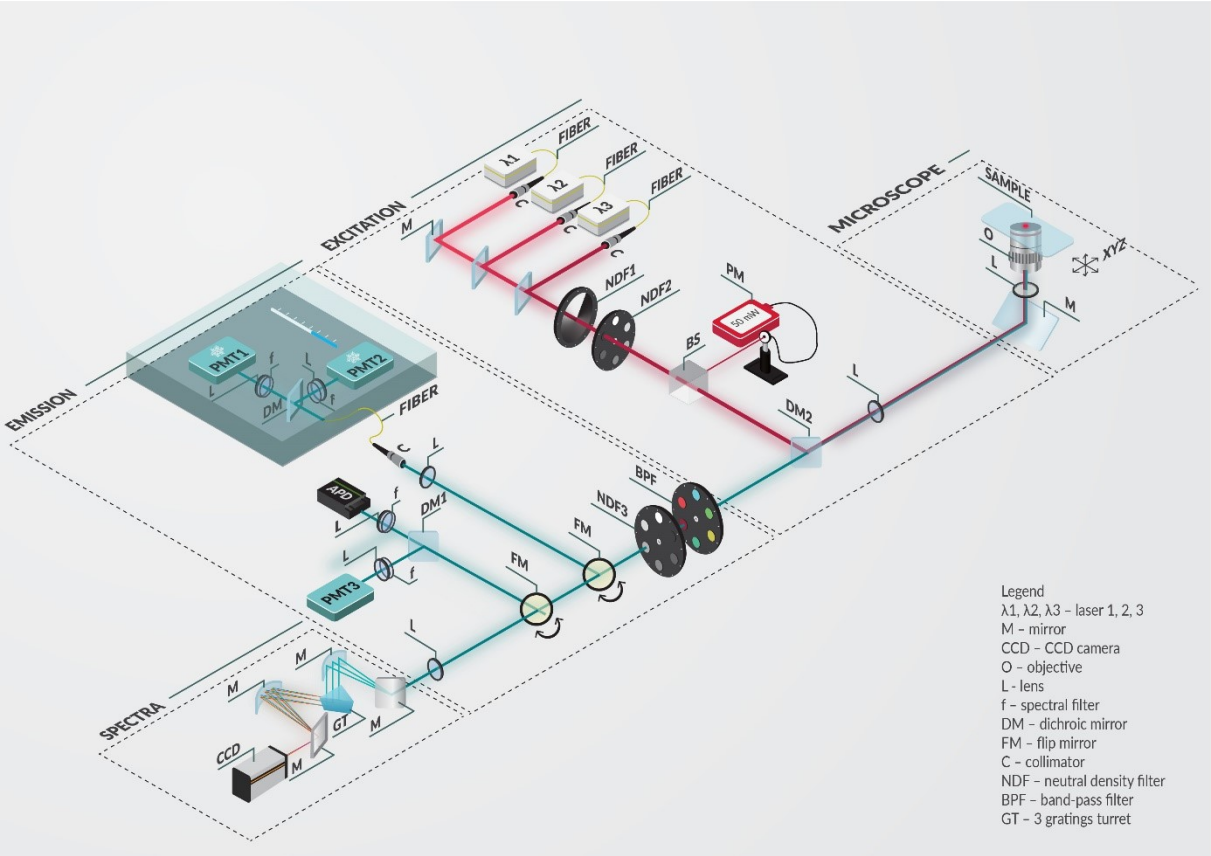

Figure S3. *Scheme of the PA optical setup*

Stokes spectra and luminescence decay

Stokes spectra were measured using a commercial Czerny-Turner photoluminescence spectrometer (FLS1000, Edinburgh Instruments), a 450W ozone-free xenon arc lamp (230-1000 nm range) and a microsecond flashlamp (200-1000 nm range) were used as excitation sources for steady state luminescence and time-resolved luminescence spectroscopy, respectively. The emission long-pass filter (400 nm) was used to cut-off scattered from the sample excitation beam. The emission beam is guided to the detector (PH) operating in 185-900 nm range and cooled to -20^{o}C in order to reduce the dark counts.

Data analysis

Data analysis such as a determination of a pump-power threshold (I_{th}) and order of nonlinearity of PA emission was performed using custom Matlab code (https://github.com/LuNASIanalysis/Photon-Avalanche-PA-).

Mean distance between nearest Tm-Nd determination

Distance between nearest Tm-Nd pairs was calculated in custom python code (https://github.com/mmajak1/average_ion_distance) using open-source Pymatgen library dedicated for material analysis (https://pymatgen.org/).

Procedure

Loading CIF file of $LiYF_4$ unit cell

Reproduction the $LiYF_4$ unit cell in 3 dimensions

Substitution of Tm and Nd ions for Y ions based on their concentration

Determination of the distance between nearest Tm-Nd pair for every Tm site

Calculating mean distance between nearest Tm-Nd

PA spectra and ET pathways determination

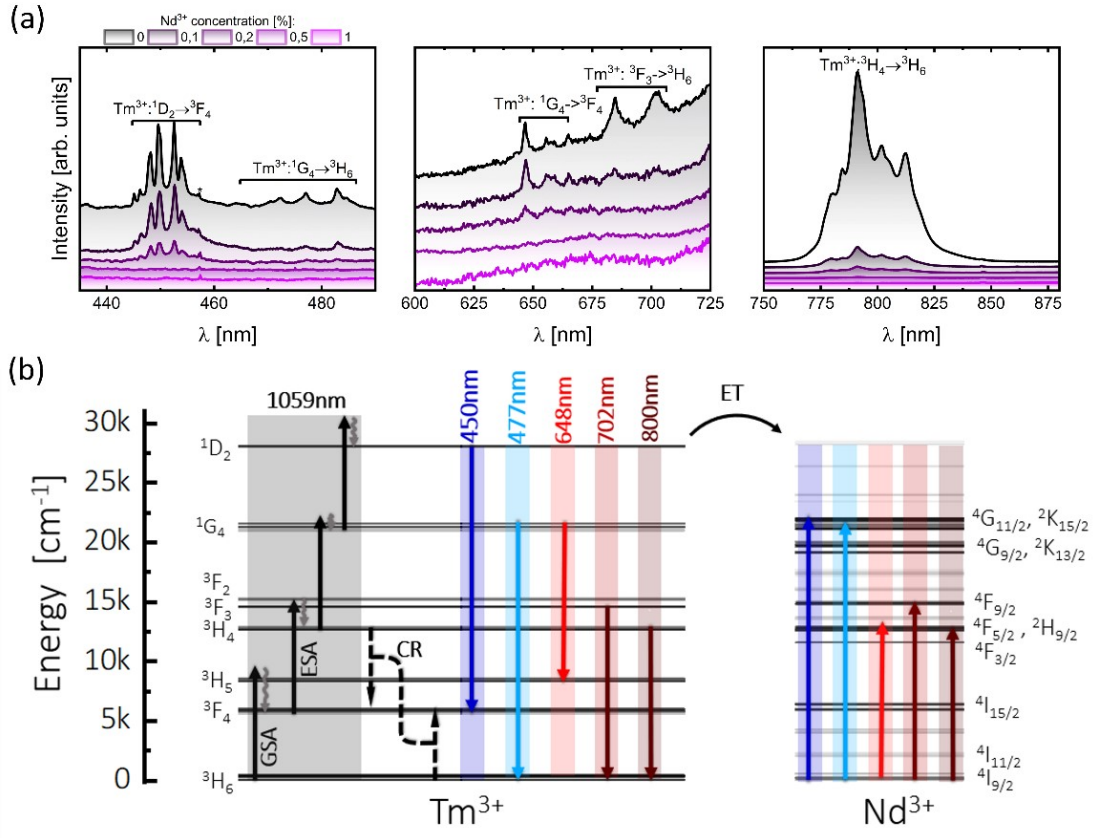

Figure S4. *(a) PA spectra collected under 1059nm excitation and 1,11*10^{7} W/cm^{2} pump power depicting five color emission bands at 450, 477, 702 and 800n. (b) Energy diagram of Tm3+ and Nd3+ showing probable energy transfer pathways.*

Table S1 *Energy transfer pathways were determined based on the experimental Tm^{3+} transition energy, considering the energy overlap with Nd^{3+} levels.*

Tm^{3+} transition (emission)	**Energy [cm^{-1}]**	**Nd^{3+} transition (absorption)**	**Energy range [cm^{-1}]** [1]
$^{1}D_2$ -> $^{3}F_4$	22222	$^{4}I_{9/2}$ -> $^{4}G_{11/2}$, $^{2}K_{15/2}$	20936 -22017
$^{1}G_4$ -> $^{3}H_6$	20964	$^{4}I_{9/2}$ -> $^{4}G_{11/2}$, $^{2}K_{15/2}$	12005 - 12677
$^{1}G_4$ -> $^{3}H_5$	15432	$^{4}I_{9/2}$ -> $^{4}F_{9/2}$, $^{2}H_{11/2}$	14246 - 16158
$^{3}F_3$ -> $^{3}H_6$	14245	$^{4}I_{9/2}$ -> $^{4}F_{9/2}$	14246 - 14966
$^{3}H_4$ -> $^{3}H_6$	12500	$^{4}I_{9/2}$ -> $^{4}F_{5/2}$,$^{2}H_{9/2}$	12005 - 12933

Supplementary discussion

Nd^{3+} ions PA-like emission under 1064 in different host materials

It is important to add, that Nd^{3+} ions have been reported to exhibit PA-like emission under 1064 nm excitation in oxide-based host materials (Y_2O_3, Gd_2O_3, $YGdO_3$, $YaIO_3$, $Y_3Al_5O_{12}$ and $LiLaP_4O_{12}$) at Nd^{3+} doping concentration of 1% at room temperature. This process was possible since $Nd^{3+:4}I_{11/2}$ level was thermally populated according to the Boltzmann distribution, allowing for further resonant $^4I_{11/2} \rightarrow {}^4F_{3/2}$ absorption and CR process populating $^4I_{15/2}$ level.[2] Through a series of multi-phonon relaxation (MPR), the $^4I_{15/2} \rightsquigarrow {}^4I_{13/2} \rightsquigarrow {}^4I_{11/2}$, the looping level becomes populated, which however may undergo the last $^4I_{11/2} \rightsquigarrow {}^4I_{9/2}$ MPR act. Therefore, thermal processes play an important role and therefore 'avalanche-like' term often describes non-resonant emission from Nd^{3+} ions under 1064 nm photoexcitation. Another Nd^{3+} PA-like emission was demonstrated in ultra-low-phonon energy heavily doped KPb_2Cl_5:16%Nd^{3+}. [3] The PA-like emission was also envisioned in $NaYF_4$:Nd^{3+},[4] although there was no successful experimental demonstration neither in $NaYF_4$ nor in different fluoride-based hosts like $LiYF_4$. In our Nd^{3+} co-doped $LiYF_4$ samples, no Nd^{3+} emission at 860 nm was found and singly Nd^{3+} doped $NaYF_4$ hosts did not exhibit typical signs of PA (data not published). Moreover, the CR based energy looping involves multiple MPR processes and the fact the $^4I_{11/2}$ looping level (energy gap to between subsequent ^4I_J, J=15/2, 13/2, 11/2 and 9/2 levels is below 2000 cm^{-1}, which is c.a. 5 times the 350 cm^{-1} cut-off phonons in (Na/Li)YF_4 host) is easily depopulated by MPR suggests that the inherent properties of Nd^{3+} ions may not be best suited for achieving PA emission. Ultimately, clearly evidenced PA emission in singly Nd^{3+} doped matrices has been successfully demonstrated only in ultra-low phonon potassium lead halide host materials (cut-off phonons <150 cm^{-1}) at RT.[3]

Based on these spectra, it seems that Nd^{3+} co-dopant does not emit (either excited directly or through Tm^{3+}) at it characteristic wavelength at 863 nm emission ($^4F_{3/2} \rightarrow {}^4I_{9/2}$), which, together with previous discussion support the hypothesis that PA process does not occur inherently in Nd^{3+} doped $LiYF_4$ at these concentrations or is inhibited by back energy transfer (Nd$\rightarrow$Tm).

Therefore, it is reasonable to assume that $\leq$ 1% Nd^{3+} ions doped in $LiYF_4$ host remains transparent under 1059 nm excitation at RT and doesn't exhibit PA like behavior by itself, supporting the idea to use Nd^{3+} ions as energy acceptors (through mechanism Q_{III}) from avalanching Tm^{3+} ions.

Power-dependent PA emission

Several power-dependent PA emissions were collected for all concentrations across various micro-crystals. The biggest fluctuations and thus deviations in electron kinetics can be observed for pristine 3%Tm^{3+} sample indicating, that Tm^{3+} ions are not distributed uniformly throughout the micro-crystal volume . These deviations are included in the PA quenching

analysis, due to the determination of the average slope and average I_{th} for all measured s-shapes.

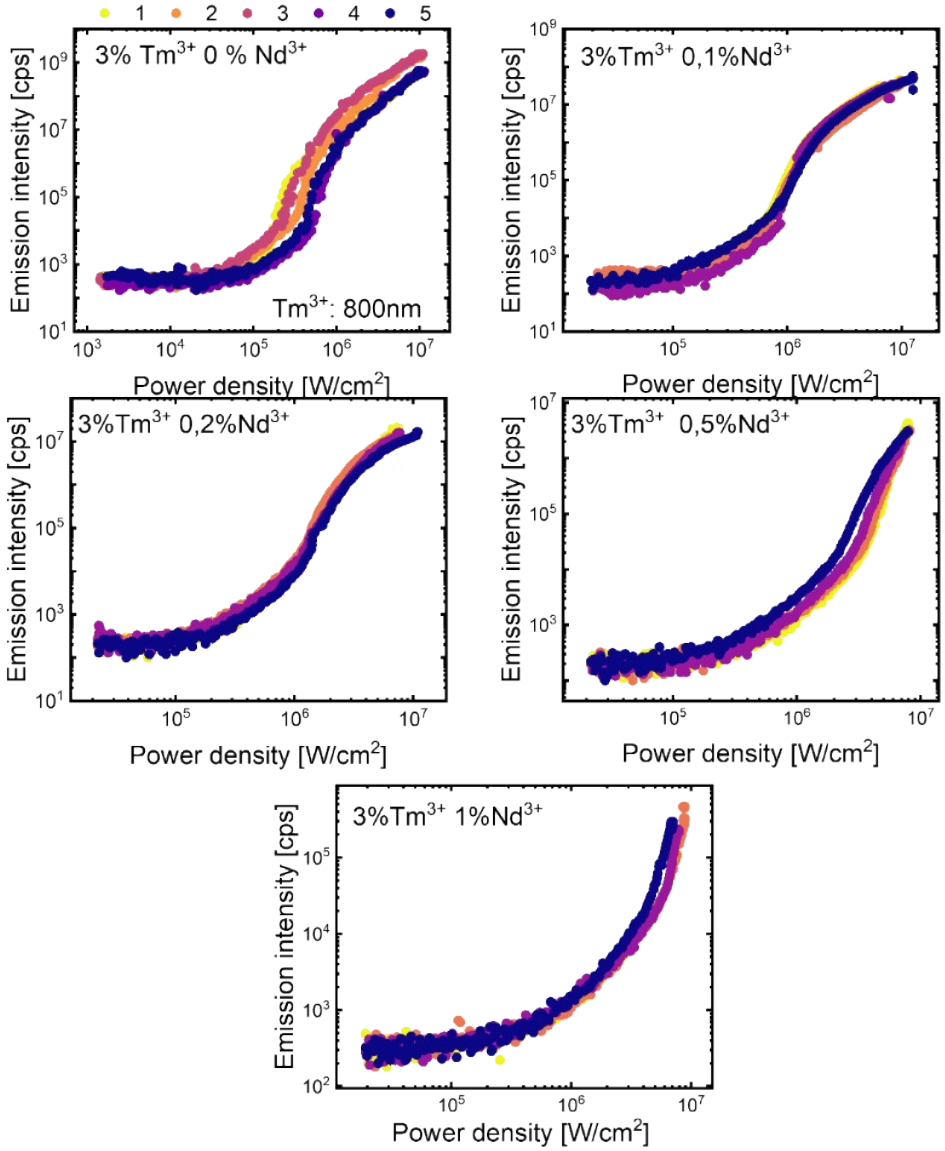

Figure S5. *Power-dependent photon avalanche emission 800nm at various Nd^{3+} concentrations (0, 0,1, 0,2, 0,5, 1%), each color depicts a measurement from a different microcrystal, illustrating variation of the s-shapes.*

Stokes emission spectra

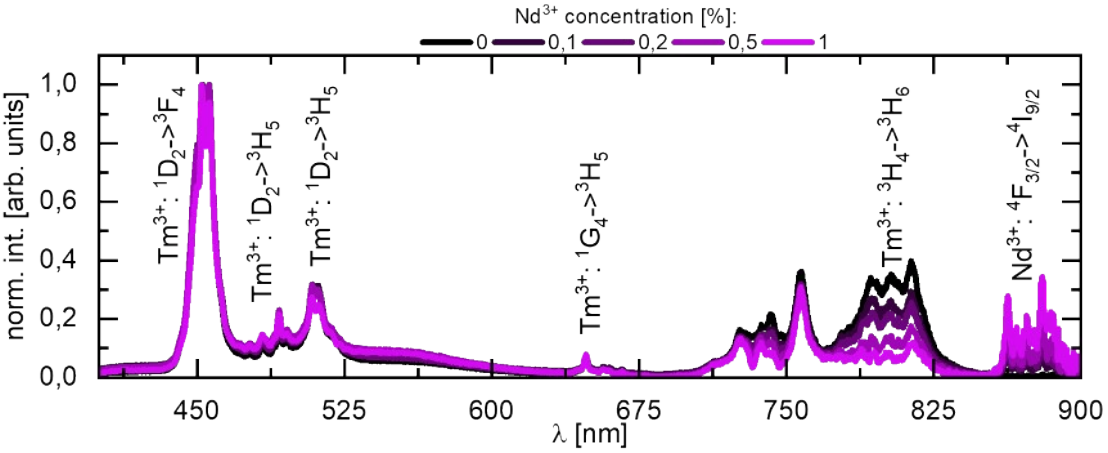

Figure S6. *Normalized to 450nm emission band Stokes spectra at various Nd^{3+} concentrations under 356nm excitation wavelength.*

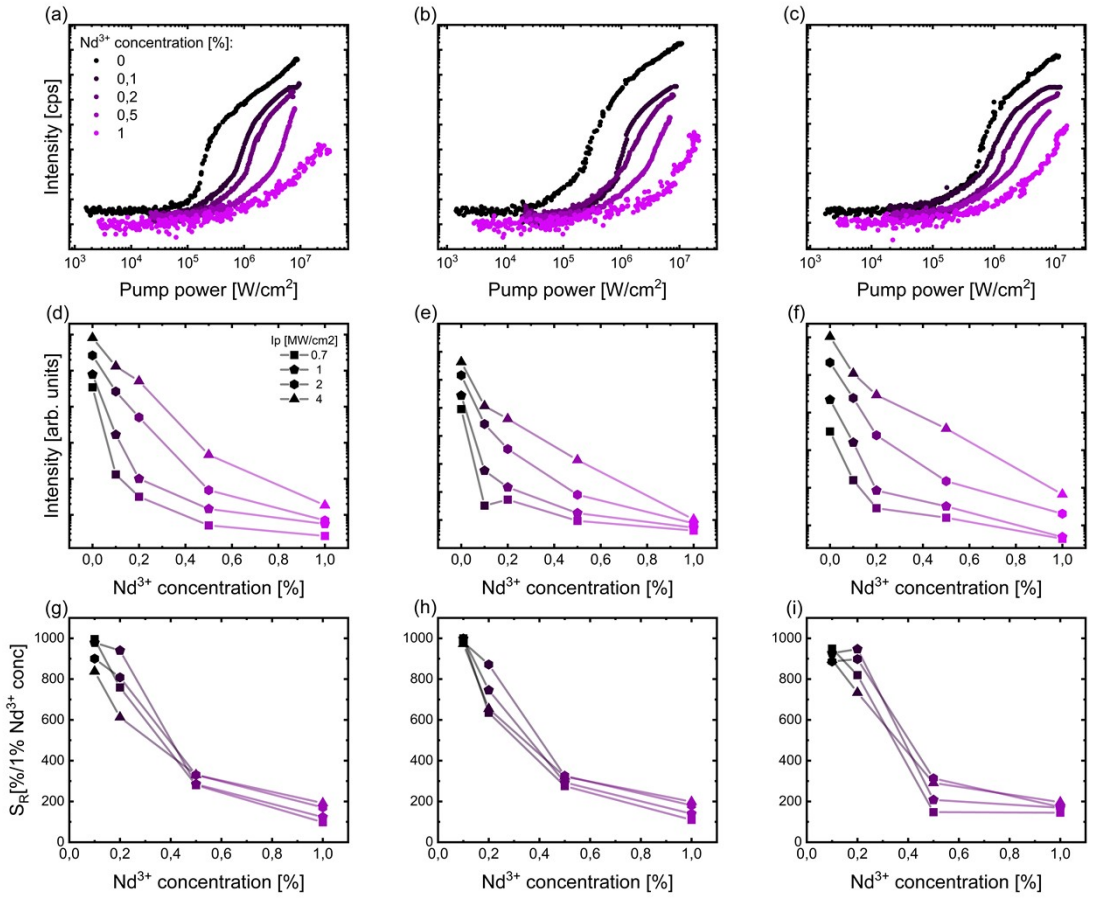

Figure S7. *(a-c) Particle-to-particle variation of pump power dependent PA emission curves (curves of the same color come from different microcrystals within the same sample batch), (d-f) corresponding emission intensity profiles at fixed pump power of 0.7, 1, 2, 4 MW cm^{-2}*

and (g-f) relative sensitivities in function of Nd^{3+} concentration, derived from experimental data presented on a,b,c, correspondingly.

Pump-probe assisted time decay measurement

Photon avalanche emission intensity is directly proportional to population of the looping state. This attribute can be exploited to probe the population and time decay of the looping state through the measurement of emitting state. Pump-probe technique usually utilizes two subsequent pulses in ultra-short time delay to measure the transmittance or reflectance in function of time delay. Here, this technique can be used to track the decay of population decay of looping state. Since lanthanides have long-living state due to the forbidden $4f^N$ transitions, the pulse and delay time duration can be in order of milliseconds to track the dynamics of the looping state. Here it can be seen that two subsequent pulses with relatively short delay of tens milliseconds between them, leads to emission intensity enhancement. With increasing delay time the enhancement of the second emission peak decreases, until the delay time is long enough that looping state population is not preserved and there's no enhancement whatsoever.

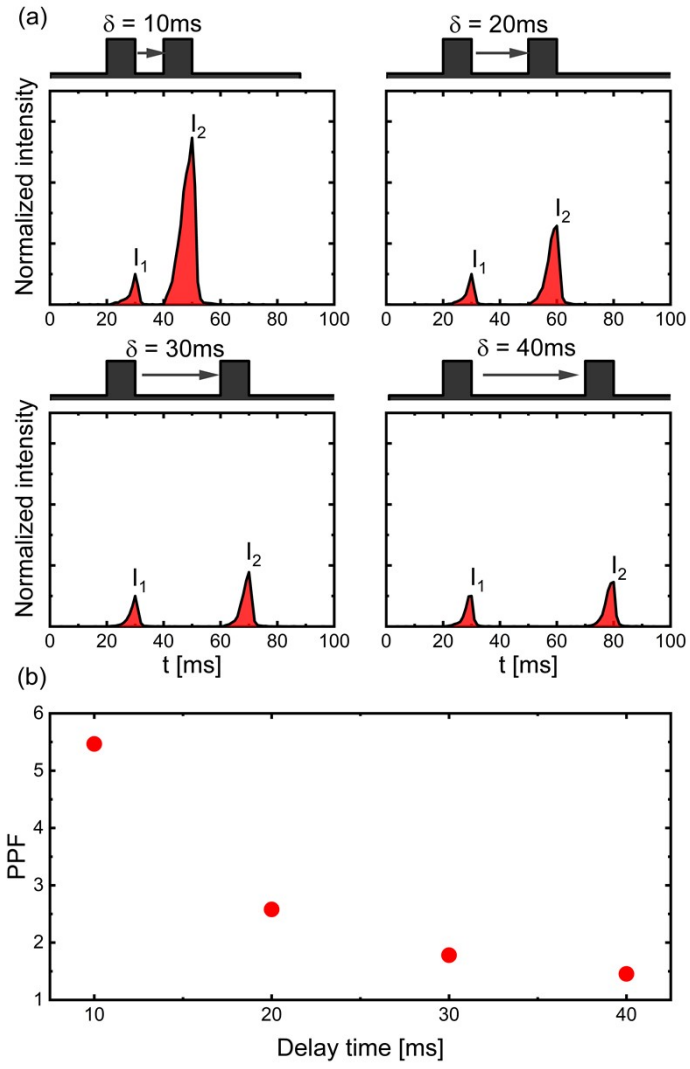

Figure S8. *(a) Demonstration of the emission intensity enhancement for two subsequent pulses with delay time δ = 10, 20, 30, 40ms and (b) ratio PPF in function of delay time carrying information on the time decay of the looping level.*

Tm^{3+} 800nm emission model based on DRE equations

Pump-power dependent photon avalanche emission can be described via a differential rate equation (DRE) based on a three-level model. Since multi-phonon relaxation processes are fast enough to neglect levels from which they occur ($^3H_5 \rightarrow {}^3F_4$, $^3F_{2/3} \rightarrow {}^3H_4$).[5] Thus, only crucial levels are taken into consideration as $^3H_6$ ground state (n_1), $^3F_4$ looping state and $^3H_4$ emitting state. This model was previously applied to fit the experimental power dependent PA emission in colloidal Tm^{3+} nanoparticles with various Tm^{3+} concentrations (4%, 8%, 20%)[6] and model the PA behavior in 8%Tm^{3+}. [7,8]

$$\frac{dn_3}{dt} = \frac{Ip}{hv}\sigma_{ESA}n_2 - (A_3 + k_3)n_3 - s_{31}n_1 + Q_{23}n_2^2 - kET_3n_3 \qquad \textbf{(Equation 1)}$$

$$\frac{dn_2}{dt} = \frac{I_p}{hv}(\sigma_{ESA}n_1 - \sigma_{ESA}n_2) - (A_2 + k_2)n_2 + (\beta_{32}A_3 + k_3)n_3 + 2s_{31}n_1n_3 - (Q_{22} + 2 - kET_2n_3$$

(Equation 2)

$$\frac{dn_1}{dt} = -\frac{dn_2}{dt} - \frac{dn_3}{dt} \qquad \textbf{(Equation 3)}$$

Here, σ_{GSA} and σ_{ESA} denote ground and excited state absorption cross-section coefficients, $k_{2(3)}$ and $A_{2(3)}$, respectively, non-radiative and radiative rate from $n_{2(3)}$. Three energy transfer processes are described as function of dopant concentration (c) $s_{31} = a_{cr}c^2$, $Q_{22} = a_{uc}\frac{c^3}{c^2 + 4.3^2}$ and $Q_{23} = a_{inv}\frac{c^3}{c^2 + 4.3^2}$. b_{32} and b_{31} parameters are branching ratios respectively from $n_3 \rightarrow n_2$ and $n_3 \rightarrow n_1$ levels.

To replicate the parasite energy transfer (ET) from the donor to the acceptor, new parameters, $k_{ET2(3)}$, indicating the ET rate leading to the depopulation of the n_2 and n_3 levels, were introduced. The ET rate was chosen arbitrarily within a range (0-1000 s^{-1}) where changes in PA behavior are most pronounced.

It must be noticed that simulation based on the simplified PADRE equations is not an ideal representation of the Nd^{3+} co-doped $LiYF_4$:3%Tm^{3+} system and allows only to model PA effect qualitatively.

Table S2. *Parameters used in DRE model (adapted from [6])*

σ_{GSA} (x 10^{-25} m^2)	6 x 10^{-4}
σ_{ESA}(x 10^{-25} m^2)	6.4
a_{cr} (s^{-1})	160
a_{uc} (s^{-1})	25.6
a_{inv} (s^{-1})	9
k_2 (s^{-1})	40.7

$\mathbf{k_3\,(s^{-1})}$	87.3
$\mathbf{A_2\,(s^{-1})}$	162.6
$\mathbf{A_3\,(s^{-1})}$	636,01
$\mathbf{b_{32}\,(s^{-1})}$	0.144
$\mathbf{b_{31}\,(s^{-1})}$	0.856

Order of nonlinearity (S) in function of power density

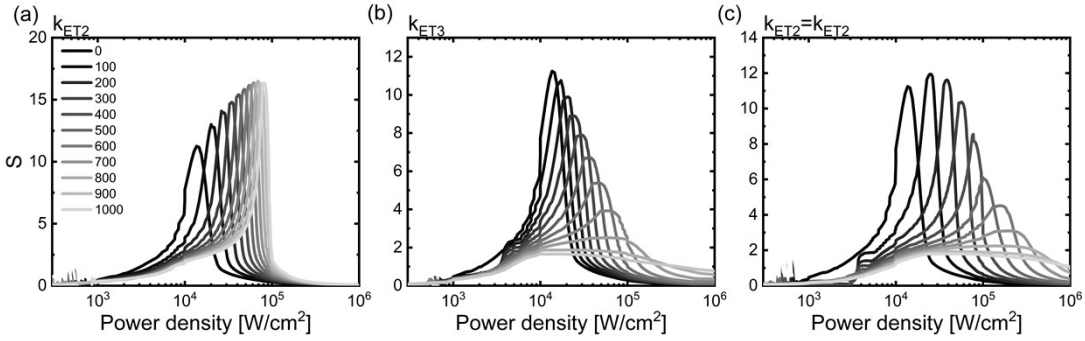

Figure S9. *Order of nonlinearity determined from simulated pump power dependent PA emissions for three quenching scenarios (a) QI, (b) QII and (c) QIII.*

Rate of change of S_{max} in function of k_{ET2} and k_{ET3}

S_{max} changes are studied in a function of k_{ET2} and k_{ET3} quenching rates (Figure S10). The increase of k_{ET3} (mechanism Q_{II}) causes an almost linear decrease of S_{max} until it achieves value close to 2 at 900 s^{-1}. Here, the k_{ET3} above 900s^{-1} quench completely the PA process and only regular up-conversion with S_{max} only up to 2 can occur. In contrast to k_{ET3}, the increase of k_{ET2} (mechanism Q_I) results in a slight increase of S_{max} up to 600s^{-1}. Nonlinearity of PA is governed by CR process, thus the higher CR rate means that PA can achieve even steeper pump power dependent emission intensity. CR is a process depending on the population of the emitting state and ground state. ET from emitting level causes decrease its population, thus CR cannot occur so effectively, what decrease S_{max}.

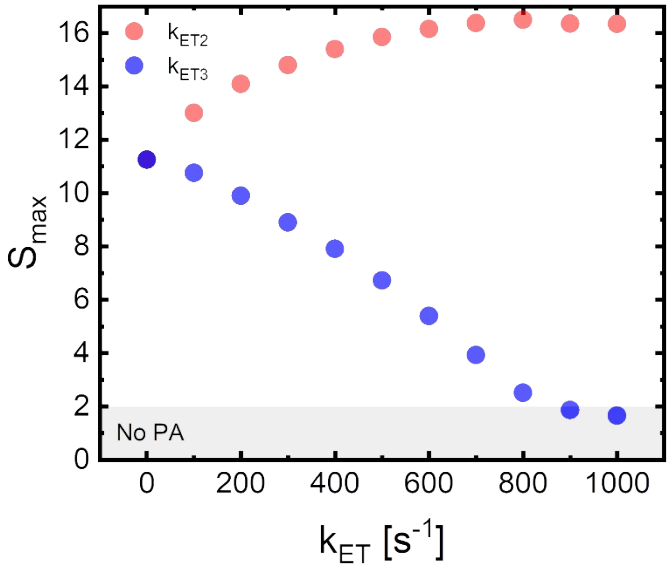

Figure S10. M*aximum order of nonlinearity of PA emission in function for two quenching scenario* Q_I *and* Q_{II} *where* $K_{ET2(ET3)}$ *= 0-1000* s^{-1} ($k_{ET3(ET2)}$*= 0* s^{-1}*).*

Intriguingly, ET from the looping state has opposite effect to ET from emitting level, since with increase of k_{ET2} rate the S_{max} starts to increase, as it would with increase of CR rate (**Figure S11**). Before the PA regime is reached, the GSA is the main process responsible for initial population of the looping state. After approaching the threshold of PA regime, CR becomes dominating process populating the looping state along with negligible GSA process. The electrons excited through GSA cannot be used in CR relaxation process, thus it concluded that GSA inhibits the CR and PA process, although it is essential to achieve the threshold looping state population. It's believed that ET from looping state allows to retrieve the electrons excited via GSA to the ground state, where they can be further used in CR process. Here, it can be seen, that not only sensitization can increase order of nonlinearity of PA, but also energy transfer occurring from the looping state, although further experimental verification is needed.

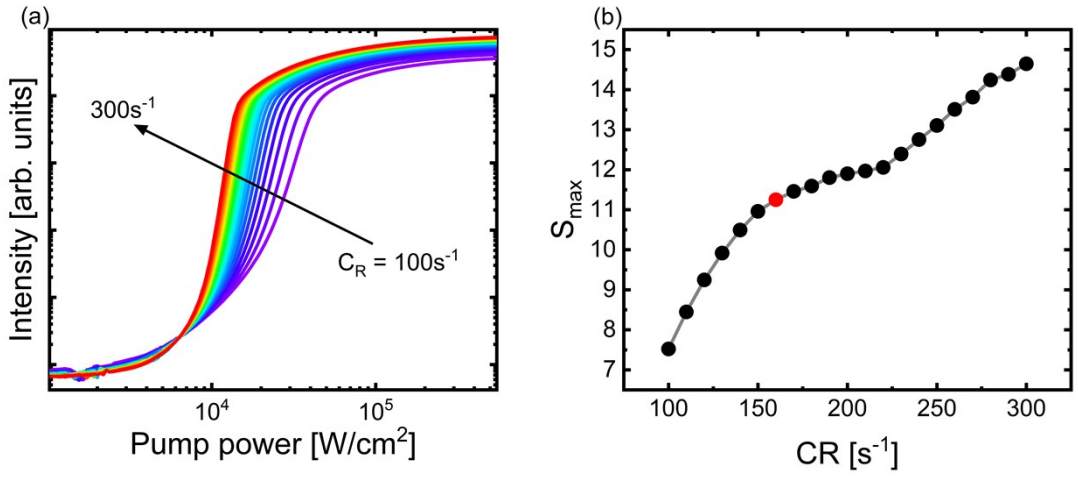

Figure S11. *(a) Power dependent PA emission in function of CR rate (100 – 300 s^{-1}) and (b) and corresponding maximum orders of nonlinearity S (default CR value used in simulations is denoted with red dot – 160 s^{-1}).*

Simulations of pump power dependent risetimes

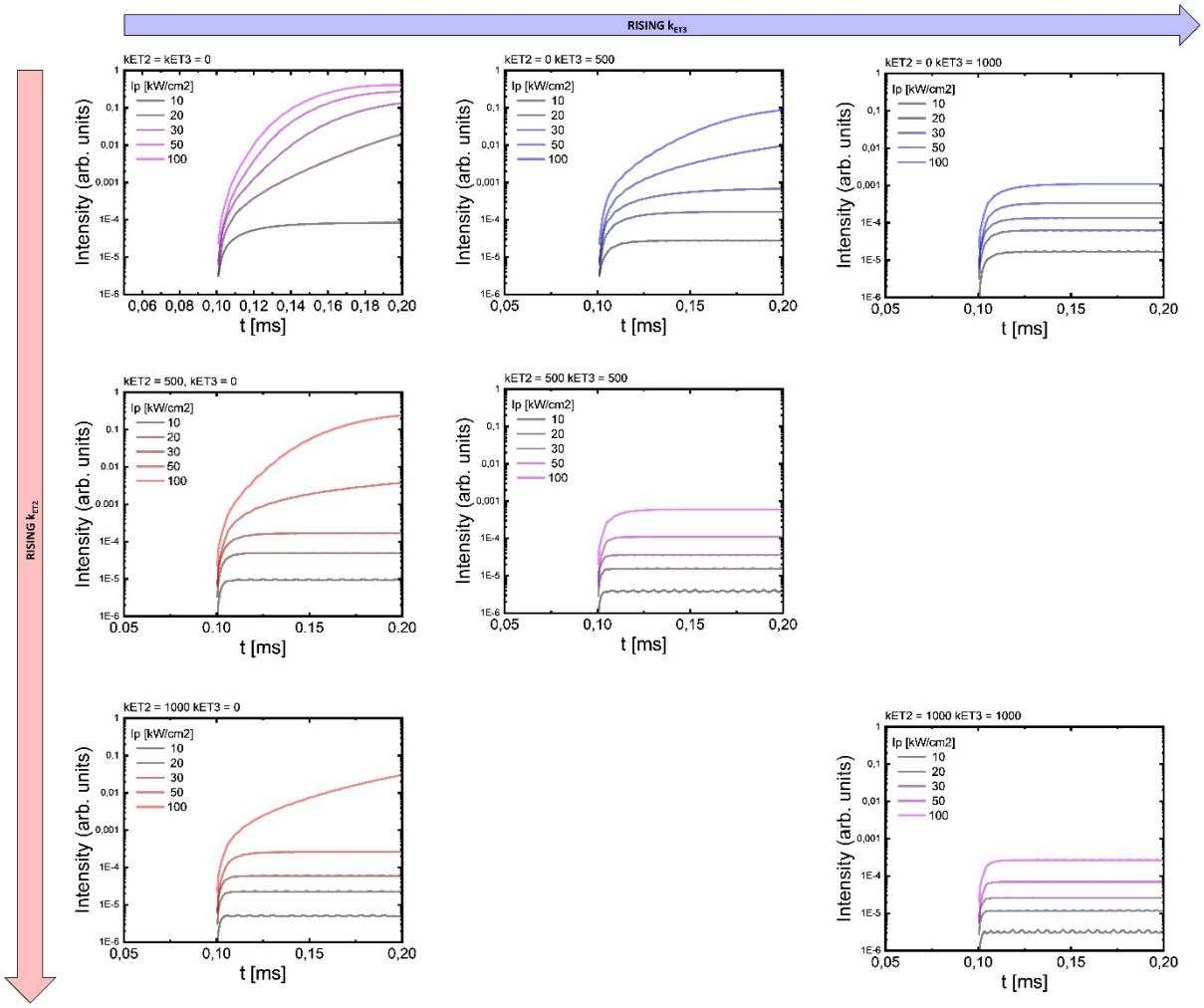

Figure S12. Simulated dependence of the pump power dependent PA risetimes for Q_I (through k_{ET2} increase), Q_{II} (through l_{ET3} increase) and Q_{III} (through simultaneous k_{ET2} and k_{ET3} increase) mechanisms.

References

1. Kaminskiĭ, A. Aleksandrovich. *Crystalline lasers : physical processes and operating schemes*. (CRC Press, 1996).

2. Marciniak, L., Bednarkiewicz, A. & Elzbieciak, K. NIR–NIR photon avalanche based luminescent thermometry with Nd3+ doped nanoparticles. *J Mater Chem C Mater* **6**, 7568–7575 (2018).

3. Zhang, Z. *et al.* Tuning Phonon Energies in Lanthanide-doped Potassium Lead Halide Nanocrystals for Enhanced Nonlinearity and Upconversion. *Angewandte Chemie International Edition* **62**, e202212549 (2023).

4. Bednarkiewicz, A., Chan, E. M., Kotulska, A., Marciniak, L. & Prorok, K. Photon avalanche in lanthanide doped nanoparticles for biomedical applications: super-resolution imaging. *Nanoscale Horiz* **4**, 881–889 (2019).

5. Joubert, M. F., Guy, S., Jacquier, B. & Linarés, C. The photon-avalanche effect: review, model and application. *Opt Mater (Amst)* **4**, 43–49 (1994).

6. Lee, C. *et al.* Giant nonlinear optical responses from photon-avalanching nanoparticles. *Nature 2021 589:7841* **589**, 230–235 (2021).

7. Bednarkiewicz, A. *et al.* All-Optical Data Processing with Photon-Avalanching Nanocrystalline Photonic Synapse. *Advanced Materials* 2304390 (2023) doi:10.1002/ADMA.202304390.

8. Dudek, M. *et al.* Size-Dependent Photon Avalanching in Tm3+ Doped LiYF4 Nano, Micro, and Bulk Crystals. *Adv Opt Mater* **10**, 2201052 (2022).